

Second-harmonic generation microscopy of photocurable polymer intrastromal implants in ex-vivo corneas

Juan M. Bueno,* Raquel Palacios, Alexandros Pennos, and Pablo Artal

Laboratorio de Óptica, Instituto Universitario de Investigación en Óptica y Nanofísica, Universidad de Murcia, Campus de Espinardo (Edificio 34), 30100 Murcia, Spain

*bueno@um.es

Abstract: A custom adaptive-optics (AO) multiphoton microscope was used to visualize the corneal stroma after the insertion of a photocurable polymer material. A lamellar pocket was created and a certain amount of polymer in liquid form was injected. This turned into a rigid film after UV irradiation. Intact eyes were used as control. Tomographic and regular second harmonic generation (SHG) microscopy images were recorded from both control and corneas with polymer implants. In control corneas, the SHG signal decreased uniformly with depth. However, treated corneas exhibited an abrupt loss of SHG signal at the implant location. The use of AO increased the SHG levels and improved the visualization of the stroma, not only at deeper corneal layers but also beneath the implant. Moreover, the absence of SHG signal from the implant allowed its geometrical characterization (thickness and location). This technique offers a potential tool for non-invasive analysis of morphological changes in the cornea after surgery or treatment, and might be useful in future clinical environments.

©2015 Optical Society of America

OCIS codes: (170.3880) Medical and biological imaging; (180.4315) Nonlinear microscopy; (110.1080) Active or adaptive optics; (170.4470) Ophthalmology.

References and links

1. P. J. Campagnola, H. A. Clark, W. A. Mohler, A. Lewis, and L. M. Loew, "Second-harmonic imaging microscopy of living cells," *J. Biomed. Opt.* **6**(3), 277–286 (2001).
2. S. Fine and W. P. Hansen, "Optical second harmonic generation in biological systems," *Appl. Opt.* **10**(10), 2350–2353 (1971).
3. A. T. Yeh, N. Nassif, A. Zoumi, and B. J. Tromberg, "Selective corneal imaging using combined second-harmonic generation and two-photon excited fluorescence," *Opt. Lett.* **27**(23), 2082–2084 (2002).
4. M. Han, G. Giese, and J. Bille, "Second harmonic generation imaging of collagen fibrils in cornea and sclera," *Opt. Express* **13**(15), 5791–5797 (2005).
5. N. Morishige, W. M. Petroll, T. Nishida, M. C. Kenney, and J. V. Jester, "Noninvasive corneal stromal collagen imaging using two-photon-generated second-harmonic signals," *J. Cataract Refract. Surg.* **32**(11), 1784–1791 (2006).
6. B. G. Wang, A. Eitner, J. Lindenau, and K. J. Halbhauer, "High-resolution two-photon excitation microscopy of ocular tissues in porcine eye," *Lasers Surg. Med.* **40**(4), 247–256 (2008).
7. S. W. Teng, H. Y. Tan, J. L. Peng, H. H. Lin, K. H. Kim, W. Lo, Y. Sun, W. C. Lin, S. J. Lin, S. H. Jee, P. T. So, and C. Y. Dong, "Multiphoton autofluorescence and second-harmonic generation imaging of the ex vivo porcine eye," *Invest. Ophthalmol. Vis. Sci.* **47**(3), 1216–1224 (2006).
8. J. M. Bueno, E. J. Gualda, and P. Artal, "Analysis of corneal stroma organization with wavefront optimized nonlinear microscopy," *Cornea* **30**(6), 692–701 (2011).
9. F. Aptel, N. Olivier, A. Deniset-Besseau, J.-M. Legeais, K. Plamann, M.-C. Schanne-Klein, and E. Beaurepaire, "Multimodal Nonlinear Imaging of the Human Cornea," *Invest. Ophthalmol. Vis. Sci.* **51**(5), 2459–2465 (2010).
10. N. Morishige, Y. Takagi, T. Chikama, A. Takahara, and T. Nishida, "Three-dimensional analysis of collagen lamellae in the anterior stroma of the human cornea visualized by second harmonic generation imaging microscopy," *Invest. Ophthalmol. Vis. Sci.* **52**(2), 911–915 (2011).
11. M. Winkler, G. Shoa, Y. Xie, S. J. Petsche, P. M. Pinsky, T. Juhasz, D. J. Brown, and J. V. Jester, "Three-dimensional distribution of transverse collagen fibers in the anterior human corneal stroma," *Invest. Ophthalmol. Vis. Sci.* **54**(12), 7293–7301 (2013).

12. H. Y. Tan, Y. Sun, W. Lo, S. J. Lin, C. H. Hsiao, Y. F. Chen, S. C. Huang, W. C. Lin, S. H. Jee, H. S. Yu, and C. Y. Dong, "Multiphoton fluorescence and second harmonic generation imaging of the structural alterations in keratoconus ex vivo," *Invest. Ophthalmol. Vis. Sci.* **47**(12), 5251–5259 (2006).
13. N. Morishige, A. J. Wahlert, M. C. Kenney, D. J. Brown, K. Kawamoto, T. Chikama, T. Nishida, and J. V. Jester, "Second-harmonic imaging microscopy of normal human and keratoconus cornea," *Invest. Ophthalmol. Vis. Sci.* **48**(3), 1087–1094 (2007).
14. W. Lo, W. L. Chen, C. M. Hsueh, A. A. Ghazaryan, S. J. Chen, D. H. K. Ma, C. Y. Dong, and H. Y. Tan, "Fast Fourier transform-based analysis of second-harmonic generation image in keratoconic cornea," *Invest. Ophthalmol. Vis. Sci.* **53**(7), 3501–3507 (2012).
15. P. Steven, M. Hovakimyan, R. F. Guthoff, G. Hüttmann, and O. Stachs, "Imaging corneal crosslinking by autofluorescence 2-photon microscopy, second harmonic generation, and fluorescence lifetime measurements," *J. Cataract Refract. Surg.* **36**(12), 2150–2159 (2010).
16. J. M. Bueno, E. J. Gualda, A. Giakoumaki, P. Pérez-Merino, S. Marcos, and P. Artal, "Multiphoton microscopy of ex vivo corneas after collagen cross-linking," *Invest. Ophthalmol. Vis. Sci.* **52**(8), 5325–5331 (2011).
17. A. Krüger, M. Hovakimyan, D. F. Ramírez Ojeda, O. Stachs, A. Wree, R. F. Guthoff, and A. Heisterkamp, "Combined nonlinear and femtosecond confocal laser-scanning microscopy of rabbit corneas after photochemical cross-linking," *Invest. Ophthalmol. Vis. Sci.* **52**(7), 4247–4255 (2011).
18. D. Chai, R. N. Gaster, R. Roizenblatt, T. Juhasz, D. J. Brown, and J. V. Jester, "Quantitative assessment of UVA-riboflavin corneal cross-linking using nonlinear optical microscopy," *Invest. Ophthalmol. Vis. Sci.* **52**(7), 4231–4238 (2011).
19. M. Hao, K. Flynn, C. Nien-Shy, B. E. Jester, M. Winkler, D. J. Brown, O. La Schiazza, J. Bille, and J. V. Jester, "In vivo non-linear optical (NLO) imaging in live rabbit eyes using the Heidelberg Two-Photon Laser Ophthalmoscope," *Exp. Eye Res.* **91**(2), 308–314 (2010).
20. G. Latour, I. Gusachenko, L. Kowalczyk, I. Lamarre, and M. C. Schanne-Klein, "In vivo structural imaging of the cornea by polarization-resolved second harmonic microscopy," *Biomed. Opt. Express* **3**(1), 1–15 (2012).
21. H.-Y. Tan, Y. Sun, W. Lo, S. W. Teng, R. J. Wu, S. H. Jee, W. C. Lin, C. H. Hsiao, H. C. Lin, Y. F. Chen, D. H. Ma, S. C. Huang, S. J. Lin, and C. Y. Dong, "Multiphoton fluorescence and second harmonic generation microscopy for imaging infectious keratitis," *J. Biomed. Opt.* **12**(2), 024013 (2007).
22. C. M. Hsueh, W. Lo, W. L. Chen, V. A. Hovhannisyanyan, G. Y. Liu, S. S. Wang, H. Y. Tan, and C. Y. Dong, "Structural characterization of edematous corneas by forward and backward second harmonic generation imaging," *Biophys. J.* **97**(4), 1198–1205 (2009).
23. N. Morishige, N. Yamada, X. Zhang, Y. Morita, N. Yamada, K. Kimura, A. Takahara, and K. H. Sonoda, "Abnormalities of stromal structure in the bullous keratopathy cornea identified by second harmonic generation imaging microscopy," *Invest. Ophthalmol. Vis. Sci.* **53**(8), 4998–5003 (2012).
24. S. W. Teng, H. Y. Tan, Y. Sun, S. J. Lin, W. Lo, C. M. Hsueh, C. H. Hsiao, W. C. Lin, S. C. Huang, and C. Y. Dong, "Multiphoton fluorescence and second-harmonic-generation microscopy for imaging structural alterations in corneal scar tissue in penetrating full-thickness wound," *Arch. Ophthalmol.* **125**(7), 977–978 (2007).
25. H. Y. Tan, S. W. Teng, W. Lo, W. C. Lin, S. J. Lin, S. H. Jee, and C. Y. Dong, "Characterizing the thermally induced structural changes to intact porcine eye, part 1: second harmonic generation imaging of cornea stroma," *J. Biomed. Opt.* **10**(5), 054019 (2005).
26. P. Matteini, F. Ratto, F. Rossi, R. Cicchi, C. Stringari, D. Kapsokalyvas, F. S. Pavone, and R. Pini, "Photothermally-induced disordered patterns of corneal collagen revealed by SHG imaging," *Opt. Express* **17**(6), 4868–4878 (2009).
27. W. Lo, Y.-L. Chang, J.-S. Liu, C.-M. Hsueh, V. Hovhannisyanyan, S.-J. Chen, H.-Y. Tan, and C.-Y. Dong, "Multimodal, multiphoton microscopy and image correlation analysis for characterizing corneal thermal damage," *J. Biomed. Opt.* **14**(5), 054003 (2009).
28. N. Morishige, T. Nishida, and J. V. Jester, "Second harmonic generation for visualizing 3-dimensional structure of corneal collagen lamellae," *Cornea* **28**(11 Suppl 1), S46–S53 (2009).
29. E. J. Gualda, J. R. Vázquez de Aldana, M. C. Martínez-García, P. Moreno, J. Hernández-Toro, L. Roso, P. Artal, and J. M. Bueno, "Femtosecond infrared intrastromal ablation and backscattering-mode adaptive-optics multiphoton microscopy in chicken corneas," *Biomed. Opt. Express* **2**(11), 2950–2960 (2011).
30. T.-J. Wang, W. Lo, C. M. Hsueh, M. S. Hsieh, C. Y. Dong, and F. R. Hu, "Ex vivo multiphoton analysis of rabbit corneal wound healing following conductive keratoplasty," *J. Biomed. Opt.* **13**(3), 034019 (2008).
31. M. Winkler, D. Chai, S. Kriling, C. J. Nien, D. J. Brown, B. Jester, T. Juhasz, and J. V. Jester, "Nonlinear optical macroscopic assessment of 3-D corneal collagen organization and axial biomechanics," *Invest. Ophthalmol. Vis. Sci.* **52**(12), 8818–8827 (2011).
32. Q. Wu and A. T. Yeh, "Rabbit cornea microstructure response to changes in intraocular pressure visualized by using nonlinear optical microscopy," *Cornea* **27**(2), 202–208 (2008).
33. Q. Wu, B. E. Applegate, and A. T. Yeh, "Cornea microstructure and mechanical responses measured with nonlinear optical and optical coherence microscopy using sub-10-fs pulses," *Biomed. Opt. Express* **2**(5), 1135–1146 (2011).
34. J. Colin, B. Cochener, G. Savary, and F. Malet, "Correcting keratoconus with intracorneal rings," *J. Cataract Refract. Surg.* **26**(8), 1117–1122 (2000).
35. Ö. F. Yilmaz, S. Bayraktar, A. Agca, B. Yilmaz, M. B. McDonald, and C. van de Pol, "Intracorneal inlay for the surgical correction of presbyopia," *J. Cataract Refract. Surg.* **34**(11), 1921–1927 (2008).
36. J. M. Bueno, E. J. Gualda, and P. Artal, "Adaptive optics multiphoton microscopy to study ex vivo ocular tissues," *J. Biomed. Opt.* **15**(6), 066004 (2010).

37. A. Pennos, I. Pentari, H. Ginis, N. Kariotakis, G. Kymionis, and I. Pallikaris, "Mechanical reinforcement of the cornea with an intrastromal in-situ photo-polymerised implant," *Acta Ophthalmol. (Copenh.)* **89**, S248 (2011).
38. E. J. Gualda, J. M. Bueno, and P. Artal, "Wavefront optimized nonlinear microscopy of ex vivo human retinas," *J. Biomed. Opt.* **15**(2), 026007 (2010).
39. M. Han, G. Giese, L. Zickler, H. Sun, and J. Bille, "Mini-invasive corneal surgery and imaging with femtosecond lasers," *Opt. Express* **12**(18), 4275–4281 (2004).
40. M. Han, L. Zickler, G. Giese, M. Walter, F. H. Loesel, and J. F. Bille, "Second-harmonic imaging of cornea after intrastromal femtosecond laser ablation," *J. Biomed. Opt.* **9**(4), 760–766 (2004).
41. B. G. Wang, I. Riemann, H. Schubert, D. Schweitzer, K. König, and K. J. Halbhauer, "Multiphoton microscopy for monitoring intratissue femtosecond laser surgery effects," *Lasers Surg. Med.* **39**(6), 527–533 (2007).

1. Introduction

Second harmonic generation (SHG) is a multiphoton imaging microscopy technique well suited to analyze collagen-based tissues [1]. The corneal stroma is a biological tissue composed of type I collagen presenting a natural noncentro-symmetric organization with a triple helix complex structure. Collagen was firstly reported to provide SHG signal in 1971 [2]. Due to its inherent optical sectioning properties, SHG imaging is a non-invasive tool to image the cornea [3] without using exogenous dyes.

The structure of the cornea has been studied with multiphoton microscopy in eyes of different species [3–8] including humans [5, 8, 9]. Recent investigations have shown the three-dimensional (3D) distribution of corneal collagen fibers (lamellae) at a high resolution [10, 11]. During the last years most clinical interests have been centered in exploring changes in stromal morphology with keratoconus [12–14] and after collagen cross-linking (CXL) procedures [15–18] used to stabilize disease progression. Although most studies used fixed or ex-vivo samples, some authors have reported preliminary in-vivo experiments [19, 20].

Corneal transparency is determined on the fibrillar level, which is below the resolution limit of SHG microscopy. Even though it is usually reduced with some pathologies, SHG microscopy has successfully been used to analyze the stroma organization even at deeper layers [21–23]. Other experiments involved corneal tissue containing scars [24] or affected by thermal damage [25–27]. Changes in the distribution of collagen fibers following corneal surgery [28–30] or mechanical tests [31], and as a function of intraocular pressure [32,33] have also been explored.

Recent corneal surgery procedures include the implantation of intracorneal rings segments [34] or small-aperture inlays [35]. These might modify the lamellar organization in a non-controllable manner and affect the corneal optical properties. To our knowledge, the response of intrastromal implants to multiphoton processes has not been studied yet. Moreover, when these are inserted into the cornea, the tissue is divided into two parts. The outer part can be easily analyzed with SHG microscopy in a regular manner. However, the inner part is located behind the implant and its visualization might be an issue since both the illumination beam (on the way in) and the emitted SHG light (on the way out) have to travel through the artificial implant. Taking this into account, the objective of this work has been to analyze the performance of SHG microscopy to image corneas implanted with intrastromal inlays. For this aim, photocurable polymer implants have been inserted in porcine ex-vivo corneas. Adaptive-optics (AO) SHG microscopy has been used to localize the implant itself, as well as to visualize the corneal collagen distribution in front of and beneath the implant at deeper stromal layers.

2. Experimental setup and procedure

2.1. SHG imaging microscopy

Specimens were imaged with a research AO multiphoton microscope previously described (Fig. 1) [36]. Nonlinear signals from the samples were generated with a 760-nm mode-locked Ti:Sapphire laser (76 MHz repetition rate, ~120-fs pulse width) and collected in a backscattered configuration through a 20x non-immersion long-working distance objective (numerical aperture 0.5). These signals included both SHG and Two Photon Excitation Fluorescence (TPEF), although the latter was only recorded for the isolated polymer sample

(see below). A photomultiplier tube (PMT) was used as detection unit. TPEF and SHG generated signals were isolated respectively by means of a broadband (FGL435, Thorlabs Inc., Newton, NJ, USA) and a narrow-band (FB380-10, Thorlabs Inc., Newton, NJ, USA) spectral filters placed in front of the PMT. Two galvanometric mirrors were used for the XY scanning operation. A DC-motor was used for optical sectioning across the sample along the Z direction. At the specimen plane, and depending on the analyzed sample, the laser power ranged between 100 and 130 mW/cm².

The multiphoton microscope incorporated an AO module composed of a Hartmann-Shack (HS) wavefront sensor (WFS150-5C, Thorlabs Inc., Newton, NJ, USA) and a gold-coated 140-actuator MEMS-type deformable mirror (Boston Micromachines, Cambridge, MA, USA). The AO module was used to compensate for the aberrations of the laser beam and the microscope optics as reported elsewhere [36]. The HS sensor sampled the laser beam wavefront with an array of microlenses (0.15-mm pitch and 3.7-mm focal length). From the HS image the corresponding wavefront aberration was estimated and expressed as a Zernike polynomial expansion up to 5th order across a 5-mm pupil. Working in closed-loop, this information was used by the deformable mirror to correct for the aberrations of incident laser beam at the entrance pupil of the microscope objective. The experimental system was completely automated and controlled through a LabViewTM custom-written software.

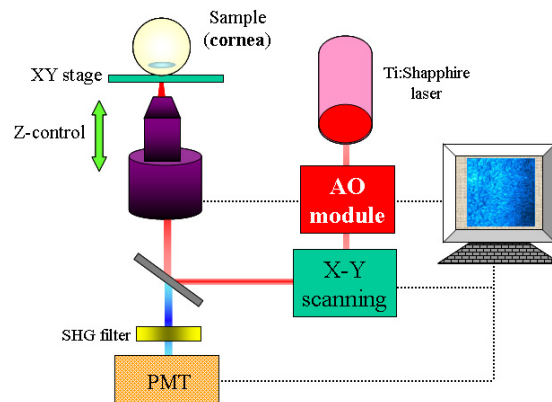


Fig. 1. AO multiphoton microscope setup. PMT, photomultiplier tube (see text for details).

2.2. Specimens

Fresh porcine eyes were obtained from a local abattoir. All animals had similar age. Ocular globes were enucleated just after death and immediately transported to the laboratory. The samples were neither fixed nor stained. All corneas appeared clear and transparent during the entire experimental session. Four eyes underwent polymer lamellar implant (see below) and multiphoton imaging. They were compared to two eyes without implantation used as control. In these control eyes, the epithelium was also removed for direct comparisons.

2.3. Polymer implant procedure

The material used as lamellar implant was a photo-polymerisable hydrophilic material (PEG/Irg). This was composed of polymer chains of poly-ethylene-glycol (average M_n 300) (Sigma Aldrich Corp., St. Louis, MO, USA) combined with a photo initiator (Irgacure 369, BASF SE, Ludwigshafen, Germany) at a proportion of 0.01% w/v (polymer to initiator). PEG/Irg material has been previously evaluated in terms of biocompatibility, toxicity and bio-mechanical effects [37]. Each cornea was firstly de-epithelialized with a mechanical brush. A diamond micrometer knife (Katena Products, Inc. Denville, NJ, USA) was used to create an initial incision of a specific depth (Fig. 2). A rounded-edge corneal scalpel was inserted through the incision, gently separating the stromal lamellae, creating a longitudinal lamellar

pocket. Following the manual pocket creation, a certain amount of PEG/Irg in liquid phase was injected in the pocket. In order to trigger the procedure of polymerization the cornea was then irradiated with a UV lamp (390 nm) for 30 seconds at a distance of 10 cm. The PEG/Irg underwent polymerization and the associated phase transition to form a rigid film.

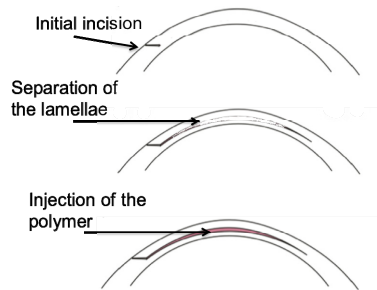


Fig. 2. Schematic representation of the insertion of the intrastromal polymer layer.

2.4. SHG imaging protocol

For SHG imaging, an entire eye (in both control and implanted) was placed upside down on a bottom-glass dish (170- μm thickness) filled with a solution of Medium 199 (Sigma Aldrich Corp., St. Louis, MO, US). This ensured that the corneal layer in contact with the cover glass was the anterior stroma (i.e. the Bowman's membrane).

Two imaging modalities with different temporal acquisition patterns [28] were used. One was the "regular" XY + Z imaging, that is, XY images for different depth locations (stacks of images). This allows the visualization of the stroma and spatially resolved analyses of changes at particular depth positions within the sample and 3D imaging. Tomographic imaging was the other imaging modality. This provides XZ images similar to the typical B-scans obtained with optical coherence tomography (OCT) techniques. Although with lower resolution, this permits a faster (~ 1 minute for this experiment) visualization of the sample's thickness, and monitoring transversal changes in morphology after treatment or manipulation. For an easier understanding, the left part of the XZ tomographic images shown in the Results section corresponds to the anterior stroma. The "zero distance" for depth imaging was chosen as the first location where SHG signal appeared. It was carefully ensured that for all specimens, the imaged areas corresponded to the central cornea.

For XY + Z imaging all samples were scanned with a 5- μm step size along the Z-axis to generate volume rendering data sets. At each corneal layer series of three SHG images were acquired. Each set of three individual XY frames (2 seconds each) was averaged to get a final image. For XZ tomographic imaging, the lateral separation was 2 μm . Image processing was performed with a custom-developed MatLab[®] software. 3D volume renderings were reconstructed from the stacks of XY images along Z-axis using ImageJ image processing software.

3. Results

The response of the polymer PEG/Irg to the mode-locked laser illumination was first tested. A drop of polymer was deposited on a microscope slide. This was polymerized using the procedure above explained and placed on the microscope for multiphoton imaging. The intensity profiles of TPEF and SHG signals were recorded across the entire sample. The results are depicted in Fig. 3. It can be observed how the SHG signal is weak. TPEF signal dominates (total TPEF intensity was more than 13-fold). Since the PEG/Irg hardly provides SHG signal, this will facilitate its localization within the corneal stroma as shown below. As a consequence there will be a lack of SHG signal when imaging the corneal areas occupied by this material compared to the strong SHG signal emitted by the corneal stroma.

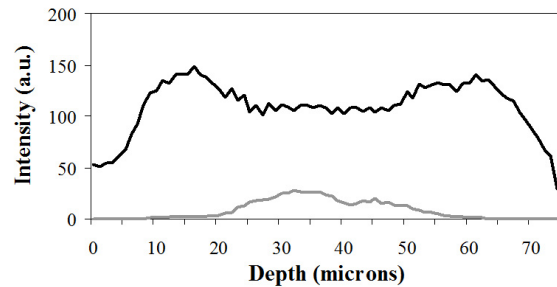


Fig. 3. TPEF (black line) and SHG (grey line) signal intensity values across a polymer sample.

To show the benefit of using AO on corneal SHG imaging, Fig. 4 presents a direct comparison of the SHG intensity profiles as a function of depth before (grey line) and after (black line) using AO. For every corneal layer the signal detected with AO in operation was higher. In particular, the use of AO enables imaging deeper layers (posterior stroma) with enough contrast to be processed. For this particular sample the difference between the maximum and the minimum intensity value was about three times larger when using AO. If AO is not used, information from deeper structures might be lost. SHG images of two individual corneal stroma layers are also included in Fig. 4. As expected, AO improves the visibility of features within the corneal stroma.

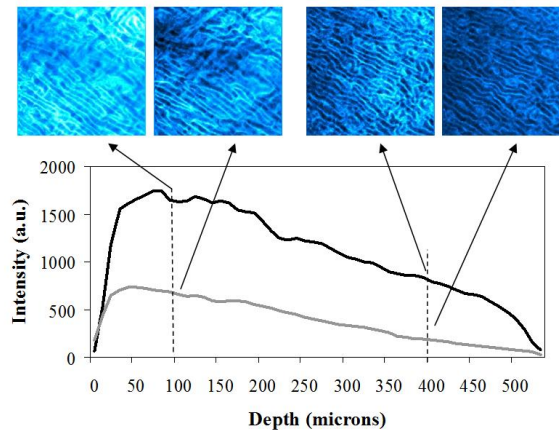


Fig. 4. Example of the benefit of AO in SHG imaging of a porcine cornea. The plot shows the SHG intensity profiles as a function of depth without (grey line) and with (black line) AO in operation. For direct comparisons SHG images corresponding to a depth location of 100 and 400 μm are also shown. Image size: $210 \times 210 \mu\text{m}^2$.

Tomographic SHG images of a porcine cornea implanted with the polymer without and with AO are shown in Fig. 5. These images were not averaged and they appear more pixelated. For each tomographic image the averaged intensity profile was also computed and is depicted in Fig. 6. These results clearly show the beneficial impact of using AO to image implants within the cornea at deeper layers. The right panels of Fig. 6 are the corresponding corneal SHG images at a depth location of 450 μm within the stroma (beneath the implant).

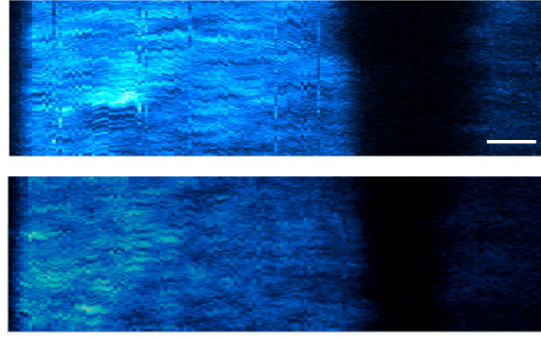


Fig. 5. Comparison of tomographic SHG images of a porcine cornea implanted with a polymer sample with AO on (upper panel) and AO off (bottom panel). Bar length: 50 μm .

Due to the weak SHG signal from the polymer implant, there is a change in intensity at the location of the inlay. This is more noticeable when using AO since the change between the edges and the center of the inlay is more abrupt (black line in Fig. 6). In addition, the SHG signals from deeper layers beneath the implant is much lower without using AO (SHG image at the bottom right) and the stromal structure can hardly be seen. The thickness and location of the intra-stromal inlay can be determined easily from tomographic images when using AO-SHG imaging (Fig. 5). On average, using AO, improvements of 3.3-fold in control corneas and 2.7-fold for corneas with implants were achieved.

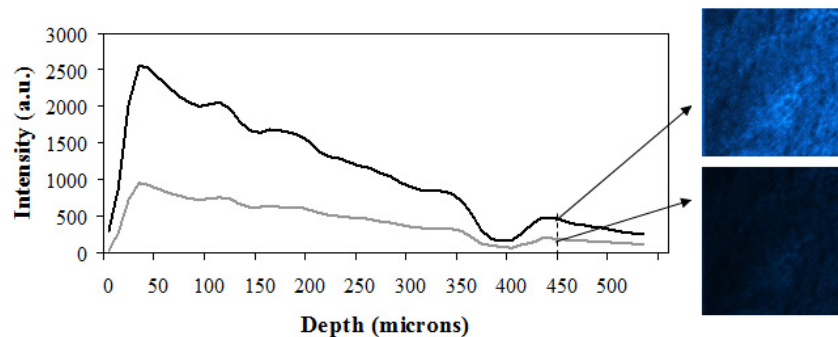


Fig. 6. Intensity profiles as a function of depth for the cornea shown in Fig. 5, without (grey) and with (black) the AO module in operation. SHG images corresponding to a depth location of 450 μm are shown on the right. Image size: 210x210 μm^2 .

Figure 7 presents two additional corneas with polymer implants located at different depth locations (about 300 and 400 μm). Even at deep locations the edges of the implant can be distinguished (see arrows).

3D representations of the corneal stroma can also be obtained from stacks of individual frames acquired along the Z direction. These provide valuable and detailed information of the tissue morphology. Figure 8 shows a volume rendering of the location and thickness of the polymer implant within the cornea. Moreover, two SHG images corresponding to two depth-positions surrounded the polymer implant have also been included. A visual inspection reveals that the lamellae present a distribution similar to that of a control cornea. This stromal organization at the adjacent areas of the polymer implant can also be observed in Fig. 9. This compares the SHG image of a cornea control (Fig. 9(a)) with another one located at a similar depth position but close to the edges of the implant (Fig. 9(b)). The corneal structure hardly loses its “normal” distribution despite the intrastromal manipulation and the implantation procedure carried out in the specimen.

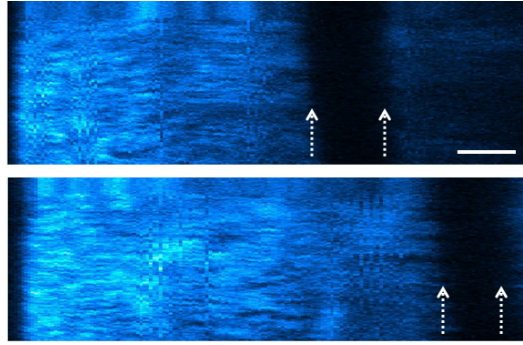


Fig. 7. Tomographic SHG images of corneas with polymer implants at different depth locations. Arrows indicate the edges of the implants. Bar length: 50 μm .

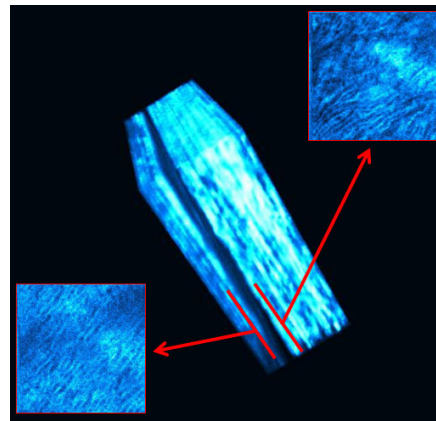


Fig. 8. Reconstructed volume rendering of an implanted porcine cornea. SHG images of the corners correspond to the locations surrounded the polymer implant as indicated by the arrows (depth locations: 375 and 445 μm , respectively).

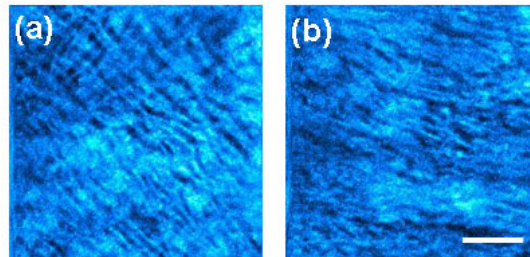


Fig. 9. SHG images of stromal collagen in a control porcine cornea (a) and in a stromal layer close to the lamellar implant of a polymer-implanted corneas (b). Both were located at similar depth position $\sim 260 \mu\text{m}$. Bar length: 50 μm .

4. Discussion and conclusions

An AO-SHG microscope has been used to visualize the corneal structure after the implantation of intrastromal polymer inlays in porcine ex-vivo eyes. SHG images of the corneal collagen were acquired in a backward configuration as a function of depth. The instrument provides a useful non-invasive imaging tool without the need of staining procedures. The use of a backscattering configuration allows multiphoton imaging of the intact ocular globe and the corneal tissue does not have to be excised (as in most previous

studies). This minimizes the effects of swelling and the appearance of edema, which modifies the normal collagen structure and may lead to erroneous conclusions.

Although the laser source was tunable, we used a wavelength of 760 nm (instead of 780 or 800 nm used by other authors) since this was the optimum wavelength for visualizing different ocular tissues (e.g. cornea, retina and lens capsule) [36, 38]. Moreover, the reason for using an on-air objective was the fact that it would be more appropriate for planned future in vivo experiments. For those in vivo experiments a coverslip will not be necessary either.

Despite intrinsic confocality properties of multiphoton processes, the recorded SHG signal decreases with depth, reducing their performance at deeper locations. The implementation of AO techniques allowed an increase in the detected SHG signal nonlinear microscopy images. These also enhanced optical sectioning properties, allowing the imaging of the entire corneal thickness (confirmed with histological measurements) and the visualization of the organization of the corneal stroma at the deepest corneal layers.

Previous studies have reported the advantages of using multiphoton microscopy to analyze the corneal structure in normal, pathological and after-surgery eyes [3–9, 28–30]. Some authors have also investigated the responses of corneal tissues to certain treatments [15–18]. In the present work, AO multiphoton microscopy has resulted in a powerful tool to visualize (and potentially evaluate) the collagen structure and its distribution after polymer corneal inlay implantation. It provides SHG images with good quality even beyond the optical zone limited by the implant. Since the polymer material used in this work hardly emits SHG signal, abrupt changes are seen between the corneal structure and the implant itself. This allows an accurate determination of the location and size of the implant within the corneal stroma. The “absence” of nonlinear signal as a result of the disruption of the collagen structure of the collagen has been previously used to visualize intrastromal corneal ablation patterns [29, 39–41]. The error in the estimation of the physical parameters of the implant depends on the distance between pairs of lines in the tomographic SHG image (2 μm for the images here used).

Although the polymer material used in this work is not currently available for clinical use [37], it allowed us to replicate to some extent the conditions of clinical intrastromal implants in the lab. The samples here used are in ex-vivo conditions, and the main goal of this work is not the analysis of the effects of the implants in the collagen distribution. However, this technique demonstrates that AO-SHG microscopy is able to visualize the spatial distribution of the stroma of any corneal layer independently of the location of the implant. Although the behaviour of living eyes might differ from that of ex-vivo eyes, this study can be considered as a starting point in the validation of microscopic changes in the stromal collagen after this kind of surgery.

In conclusion, this study has shown the effectiveness of AO-SHG microscopy to localize corneal implants and visualize the morphology of the corneal stroma at deeper layers, even beneath the implant. The absence of SHG signal at the implant location allows the assessment of its dimensions and locations within the corneal stroma. The combination of a backscattered configuration, a non-immersion objective and an AO module might make the herein instrument suitable for a future clinical environment, especially oriented to the analysis of living eyes. Pathology following-up, diagnosis and wound healing monitoring, among others, would benefit from this technique.

Acknowledgments

This work has been supported by SEIDI-Spain, grant FIS2013-41237-R and European Research Council Advanced Grant ERC-2013-dG-339228 (SEECAT). Authors acknowledge Dr. H. Ginis for helpful suggestions and collaboration during the experimental part of this work.